

Current Advances in Computational Lung Ultrasound Imaging: A Review

Tianqi Yang,^{1, a} Oktay Karakuş,^{1, b} Nantheera Anantrasirichai,^{1, c} and Alin Achim^{1, d}

¹ *Visual Information Laboratory, University of Bristol, Bristol BS1 5DD, U.K.*

(Dated: 24 December 2024)

In the field of biomedical imaging, ultrasonography has become increasingly widespread, and an important auxiliary diagnostic tool with unique advantages, such as being non-ionising and often portable. This article reviews the state-of-the-art in medical ultrasound image computing and in particular its application in the examination of the lungs. First, we review the current developments in medical ultrasound technology. We then focus on the characteristics of lung ultrasonography and on its ability to diagnose a variety of diseases through the identification of various artefacts. We review medical ultrasound image processing methods by splitting them into two categories: (1) traditional model-based methods, and (2) data driven methods. For the former, we consider inverse problem based methods by focusing in particular on ultrasound image despeckling, deconvolution, and line artefacts detection. Among the data-driven approaches, we discuss various works based on deep/machine learning, which include various effective network architectures implementing supervised, weakly supervised and unsupervised learning.

Pages: 1–26

I. INTRODUCTION

In recent years, with the development of ultrasound (US) along with the advancement of medical imaging technologies, the examination and treatment performance of US in clinical applications, especially in the diagnosis of lung diseases, has gradually been recognized and accepted by clinicians. It has changed disease treatment, prognosis and patient management, and has become a visual stethoscope and diagnosis tool that doctors can make use of. US examination has become an important medical imaging method, and it is an effective

supplement to modalities such as chest X-ray, chest computed tomography (CT), bronchoscopy, and magnetic resonance imaging (MRI). Compared with other common medical imaging modalities, US bears various advantages such as:

- (1) **Safe and non-invasive.** US imaging does not involve ionising radiation. It can hence be safely used for investigations on children and pregnant patients¹.
- (2) **Cost effective.** It enables patients to obtain accurate diagnosis without needing expensive, complicated, and invasive examinations.
- (3) **Portable.** Compared to CT, US can lessen the need for transferring critically ill patients².

^aqc18229@bristol.ac.uk

^bo.karakus@bristol.ac.uk

^cn.anantrasirichai@bristol.ac.uk

^dalin.achim@bristol.ac.uk

- (4) **High repeatability.** US allows for repeated procedures at the patient's bedside to monitor the progress of treatment.
- (5) **Real-time.** US equipment can be used for dynamic imaging and hence boost doctor's diagnostic efficiency.
- (6) **Hygiene.** US equipment is easy to clean and disinfect, particularly in the case of hand-held devices³.

Despite all these advantages, it is worth noting that US remains an auxiliary tool after all since it has limitations that cannot be easily overcome:

- (1) US is operator-dependent, and the image quality may vary due to the clinicians' skills and the precision of the device. Moreover, the interpretation of US imagery is subjective, in that the individual observation, the movement of the probe, and the parameter settings of the device effect image analysis.
- (2) The operating environment also restricts US examination. For example, critically ill patients need a variety of equipment (such as ventilators, blood purification tubes, chest drainage tubes, etc.) for life maintenance, which negatively affects US diagnosis accuracy.
- (3) Specific patient conditions also influence the US examination performance, in particular obesity, thoracic deformity, skin lesions etc. For example, in obese patients, thick subcutaneous fat may lead to serious distortion, resulting in errors in US examination. All these might influence US imagery characteristics, and affect the results of clinical examination⁴.

In this paper, we specifically review Lung US (LUS), since lung disease is one of the most severe health problems causing the death of more than 100 thousand people in the UK every year⁵. According to the British Lung Foundation, somebody dies due to lung disease in the UK every five minutes⁵. Lung disease is in fact the third

common cause of death in the UK after heart disease and cancer⁵. After the start of COVID-19 pandemic in 2020, analysis and diagnosis of lung disease became even more crucial. A rising demand for timely and correct diagnosis, as well as an increasing need for patient monitoring, have been spurred⁶.

LUS has been increasingly used to diagnose lung diseases. This is not only because of the advantages mentioned above, but LUS also helps in assessing the fluid status of patients in intensive care as well as in deciding management strategies for a range of conditions. The common feature in all clinical conditions, both local to the lungs (e.g. pneumonia, chronic obstructive pulmonary disease (COPD)) and those manifesting themselves in the lungs (e.g. kidney disease, COVID-19) is the presence in LUS of a variety of artefacts, known as A-, B-, and Z-lines. These carry important information about the severity of diseases. Thence, the majority of research conducted in this area starts from detecting and quantifying linear features in LUS images. A-lines are a kind of artifact caused by multiple reflection of sound waves due to the difference of acoustic impedance between the pleura and the lung. Their presence are indicative of a healthy lung, whereas B-lines can indicate many diseases, and characteristics such as their quantity or thickness are directly related to the severity of the disease.⁷ Therefore, the quantification of B-lines can help with assessing the particular disorder⁸. Z-lines are a type of artifact similar to B-line. The main difference consists in that Z-lines are stationary and present brightness attenuation. Occasionally, they can be seen in pneumothorax. The position of an artifact relative to the pleural line (which is the echo reflection formed by the surface of visceral and parietal pleura) is also important in determining whether the detected artifact is a B-line or merely air or another foreign body⁹. Therefore, in some studies, the pleural line is used as reference for the positioning of other line artefacts^{10,11}.

Considering the aforementioned importance of line artefacts, the literature spans various works focused on some standardized approaches of the assessment process involving LUS. For instance, the first published attempt at computerized B-lines scoring employed the 4-SCORE rule¹². This principle is however not reliable in practice, so clinical diagnosis requires more accurate evaluation standards¹³.

In the computational LUS imaging literature, traditional model-based methods are widely studied. Typically, they involve solving an inverse problem where a set of unknown deterministic parameters which are observed through a linear transformation and corrupted by additive noise are estimated¹⁴. Despite their capability to produce results by just utilising a single corrupted image, the main disadvantages of such traditional approaches are that the prior distributions are handcrafted, and the generalization ability of the models is limited. In addition, compared to other commonly used imaging modalities such as CT, X-ray and MRI, the resolution and visual quality of US images are lower. Recently, data-driven methods which mainly exploit machine learning (ML) and deep learning (DL) in particular can effectively improve the quality of US images, so they have gained increased attention.

This paper aims to provide a complete review of the current advances on computational LUS imaging methodologies. We discuss modern equipment for medical US image acquisition in Section II, and then describe the basic features and clinical applications of LUS imagery in Section III. In Section IV, processing methods for medical LUS images are presented in two sub-categories, namely the model-based and the data-driven methods. The discussions in Section V serve the purpose of summarising the whole contribution. Since current state of LUS development has not yet reached maturity, this review aims to provide inspiration and references for

the development of yet more accurate and efficient computational LUS imaging approaches.

II. ULTRASOUND IMAGING

This section is intended to provide an overview of medical ultrasound imaging, mainly in terms of instrumentation involved. While the discussion is for its more part generic, we attempt to offer clear pointers to what is relevant to LUS in particular.

A. From sound to images

Medical US is an imaging modality that uses the difference of physical characteristics of ultrasonics and acoustic properties of human organs and tissues to display and record the information in the form of waveform, curve or image. Different human organs and tissues have their specific acoustic impedance and attenuation characteristics. When sound waves are transferred into the body, their reflection and attenuation will vary from organ to organ. According to their intensity, the received echoes can be envelope detected and displayed, and hence cross-sectional US image of human body can be formed¹⁵. It took a long time before US has been adopted for imaging the lungs, as ribs, sternum and pulmonary parenchyma filled with air are structures that reject ultrasonic waves¹⁶.

A widely accepted linear model of US image formation was proposed in Ng et al.¹⁷ based on the physical propagation characteristics of sound waves. The received signal in the time domain is expressed as

$$r(\mathbf{r}_0, t) = h(\mathbf{r}, t) \otimes f_m(\mathbf{r})|_{\mathbf{r}=\mathbf{r}_0} \quad (1)$$

where \mathbf{r}_0 represents the surface of the receiver, \mathbf{r} refers to the location of the imaged tissue, $f_m(\mathbf{r})$ is the tissue reflectivity function (TRF), and $h(\mathbf{r}, t)$ refers to the system point spread function (PSF).

B. Instrumentation

Depending on clinical application, working principles, tasks and operating systems, medical US images can be acquired using various modes as follows¹⁸.

- (1) **A-mode:** When the signal returns from the tissue interface, its amplitude is directly displayed on the screen. The abscissa of the screen represents the reflected US intensity. The propagation time corresponds to the detection depth, and the ordinate represents the amplitude of the returned echo - this is called A-mode (amplitude mode) ultrasound.
- (2) **M-mode:** This acquisition mode adds the echo information obtained by the A-mode method to the Cathode-ray tube (CRT) through brightness modulation, and expands it on the time axis to obtain the trajectory of the motions. This is especially suitable for the examination of the heart and other dynamic organs.
- (3) **B-mode:** This is the most widely used US acquisition mode and the one relevant to LUS. It uses the amplitude of the echo pulse to modulate the brightness of the display. The abscissa and ordinate of the display correspond to the position of the sound velocity scan, thus forming an ultrasonic cross-sectional image modulated by the brightness. It is therefore called B-mode (brightness mode). Different types of B-mode scanners exist, including *i.* manual scanners, *ii.* real-time scanners, *iii.* mechanical scanners, *iv.* electronic scanners, with both linear-array scanners and phased-array scanners¹⁹.
- (4) **D-mode:** This uses the Doppler effect to detect the motion information of the human tissue. The Doppler detection method includes continuous wave Doppler (CW) and pulse Doppler (PW).
- (5) **C-mode** and **F-mode** ultrasonic imagers: The probe movement in C-mode and the synchronized scanning form a "Z" shape, and the displayed sound

image is perpendicular to the direction of the sound beam, which is similar to X-ray tomography. F-mode imagers are a type of C-mode imagers, which are able to reconstruct three-dimensional images.

Among all these possibilities, for LUS, M-mode and B-mode are the two most commonly used for diagnosis. Various types of probes are used in conjunction with different devices to receive and transmit ultrasonic signals. Probes are the actual ultrasonic transducer, which employ the piezoelectric effect to perform the bidirectional conversion of mechanical waves into electrical signals and vice versa. A non-exhaustive list of most commonly used clinical probes is given in the following²⁰

- (1) **Electronic convex array probes:** These are commonly used for abdominal examinations, obstetrics and gynecology examinations. Their typical working frequencies are 3 ~ 5MHz whereas, 5 ~ 10MHz are recommended for children examinations at depths of more than 30cm. Small convex array probes are used for transcranial scanning, with 1.5 ~ 3.5MHz for adults, 3.5 ~ 7.5MHz for infants and newborns under the age of 3.
- (2) **Electronic linear array probes:** Their working frequencies are over 7.5MHz, being often used for shallow investigations such as peripheral blood vessels and superficial organs.
- (3) **Electronic phased array probes:** They can be used for adult and pediatric heart examinations under working frequencies of 2 ~ 5Hz.
- (4) **Transluminar probes:** (including transesophageal, transcatheter, and endoscopic probes, etc.) They work at high frequency and can be used directly on the surface of organs or close to organs, clearly displaying the tissue structure and avoiding the interference due to depth or other organs.

Probe selection is decided by the desired tissue penetration as shown by². For the observation of in-depth lesions, low-frequency convex array probes or low-frequency phased array probes are usually selected, whereas high-frequency linear array probes are used for superficial pleural or sub-pleural detection. Image resolution increases with frequency, at the cost of penetration depth²¹.

Ultrasound scanners adapted to lung investigations have been developed by a number of vendors, including the Canon Xario Series²², Aplio Series (by GE)²³ or ²⁴. In order to satisfy eventual point-of-care (PoC) needs, many of these vendors have been developing portable devices. One such additional example is the Butterfly iQ+, which is able to perform whole body imaging with one small probe as well as provide real-time in-app monitoring.

III. CLINICAL APPLICATIONS

This section describes clinical applications of LUS imaging by reviewing the basic principles, signs, and conditions related to human lungs.

A. Lung Signs

The lungs are the main air-containing organs of the human body. In a pathological condition, the air-liquid ratio in the lungs changes, and abnormal artifacts may appear during a US examination. The analysis of LUS images is based on these signs, which are basically classified under 5 different categories, namely (i) normal lung signs (bat sign, pleural sliding, A-line), (ii) pleural effusion signs (quadrilateral sign, sine wave sign), (iii) lung consolidation signs (Fragment sign, tissue-like sign), (iv) interstitial syndrome (pulmonary rocket sign) and (v) pneumothorax (stratospheric sign, lung point)¹. Some example LUS images showing these signs are shown in Figures 1 and 2.

- **Bat sign:** If the probe is perpendicular to the ribs, the upper and lower adjacent ribs, the shadow of the ribs, and the pleural line together form a peculiar appearance called the bat sign.
- **Pleural line and pleural sliding:** In B-mode, if the probe is placed perpendicular to the body surface, the linear high echo below the ribs constituting the pleural line can be seen. The relative motion of the parietal pleura and the visceral pleura forms a reciprocating movement with breathing, which shows that the lungs are sliding relative to the chest wall when breathing.
- **A-line:** In B-mode, A-lines are a series of hyperechoic lines that are equally spaced and parallel to the pleural line and occur below the pleural line.
- **Seashore sign and sand beach sign:** In the case of lung movement with breathing, in M-mode, a uniform granular shape is formed below the pleural line, similar to a beach, called the “sand beach sign”, while the chest wall determines parallel lines due to its static state.
- **B-line or the comet tail sign:** The B-line or comet tail sign is a vertical artifact with clear boundaries and moving synchronously with lung sliding. The appearance of several B-lines in the image is also called the “rocket sign”²⁵.
- **Lung consolidation and atelectasis:** The echogenic US appearance of the lungs is similar to that of the liver or spleen.
- **Bronchial inflation sign:** In uneven tissue-like consolidation, bronchial-like linear hyperechoic signals can often be found, indicating that there is residual air in the consolidated or atelectic lung. This type of appearance is called “Bronchial inflation sign”.
- **Lung points:** A lung point is a dividing point seen in real-time ultrasound where the lung sliding exists and disappears alternately with breathing movement.
- **Pleural effusion:** When effusion occurs in the pleural cavity, the space between the visceral pleura and the

parietal pleura is filled with fluid, thereby forming a hypoechoic sign.

- **Curtain sign:** As air-filled lung moves up and down with the breathing motion and other abdominal organs are covered periodically. This is when “curtain sign” occurs.

B. Lung conditions

LUS provides a high amount of useful real-time information on changes of lung morphology. Indirect signs in LUS, such as the occurrence of abnormal pleural line, disappearance of A-lines, unexpected increase on the number of B-lines, or lung consolidations, can reveal the severity of lung disease. In the following we include a non-exhaustive list of lung diseases, observable with LUS, along with their peculiar abnormalities.

- (1) **Pleural effusion:** The use of (M-mode) LUS in the diagnosis of pleural effusions dates back to 1967²⁰. In the evaluation of pleural effusion, LUS is highly sensitive to small amounts of fluid. When the acoustic impedance between the media is greater than 0.1%, US echo reflections appear. The quadrilateral sign is another important characteristic manifestation of M-mode LUS in the diagnosis of pleural effusion, with a sensitivity of 93% and a specificity of 97%¹.
- (2) **Pneumothorax:** The initial sign of a pneumothorax is the disappearance of the pulmonary sliding sign. Instead of the beach sign, the M-mode LUS shows a superposition of parallel lines that lack motion characteristics. M-mode imaging can clearly identify lung signs, with the diagnostic specificity of 100% and the sensitivity of 66%. For occult pneumothorax the sensitivity values would reach up to 79%¹.
- (3) **Pneumonia & COVID-19:** The main manifestations of pneumonia are varying degrees of lung consolidation and abnormal pleural lines, some with fu-

sion of B-lines and pleural effusion. Pneumonia can be characterized by B-lines, the quantity and characteristics of which vary according to the severity of the disease²⁶. A previous work by Chavez *et. al.*²⁷ shows that LUS had a high sensitivity (94%) and specificity (96%) for the diagnosis of pneumonia in adults, demonstrating that LUS is a reliable tool in diagnosing pneumonia.

Nowadays, the world is exposed to the COVID-19, a condition which sometimes induces pneumonia and has high infection rates. Recent studies^{6,28,29} summarize the symptoms of COVID-19 patients into several points all of which can be identified with LUS. These are: *i.* B-lines begin to increase in number and distribution. *ii.* The pleural line begins to become irregular. *iii.* Areas with B-lines are adjacent to normal areas of lung sliding and A-lines. *iv.* There are ‘skip lesions’ or ‘spared areas’. *v.* Small consolidations around the lung.

- (4) **Chronic obstructive pulmonary disease (COPD):** COPD is listed as the fourth major cause of human death by the World Health Organization (WHO). The ultrasonographic features of COPD include pulmonary A-line, pulmonary sliding sign and no right ventricular overload²⁰.
- (5) **Acute respiratory distress syndrome (ARDS):** It has been shown in a previous study²⁰ that ARDS accounts for 10.4% of ICU patients, and the mortality rate due to severe ARDS is as high as 40%. The symptoms of ARDS mainly include lung consolidation with bronchial inflation sign, abnormal pleural line, diffuse pulmonary edema, and disappearance of A-lines. Different from the diagnostic criteria defined in Berlin for ARDS³⁰, a new study pointed out that EVLW (extravascular lung water) is more reliable as a new indicator to classify the severity of ARDS³¹.

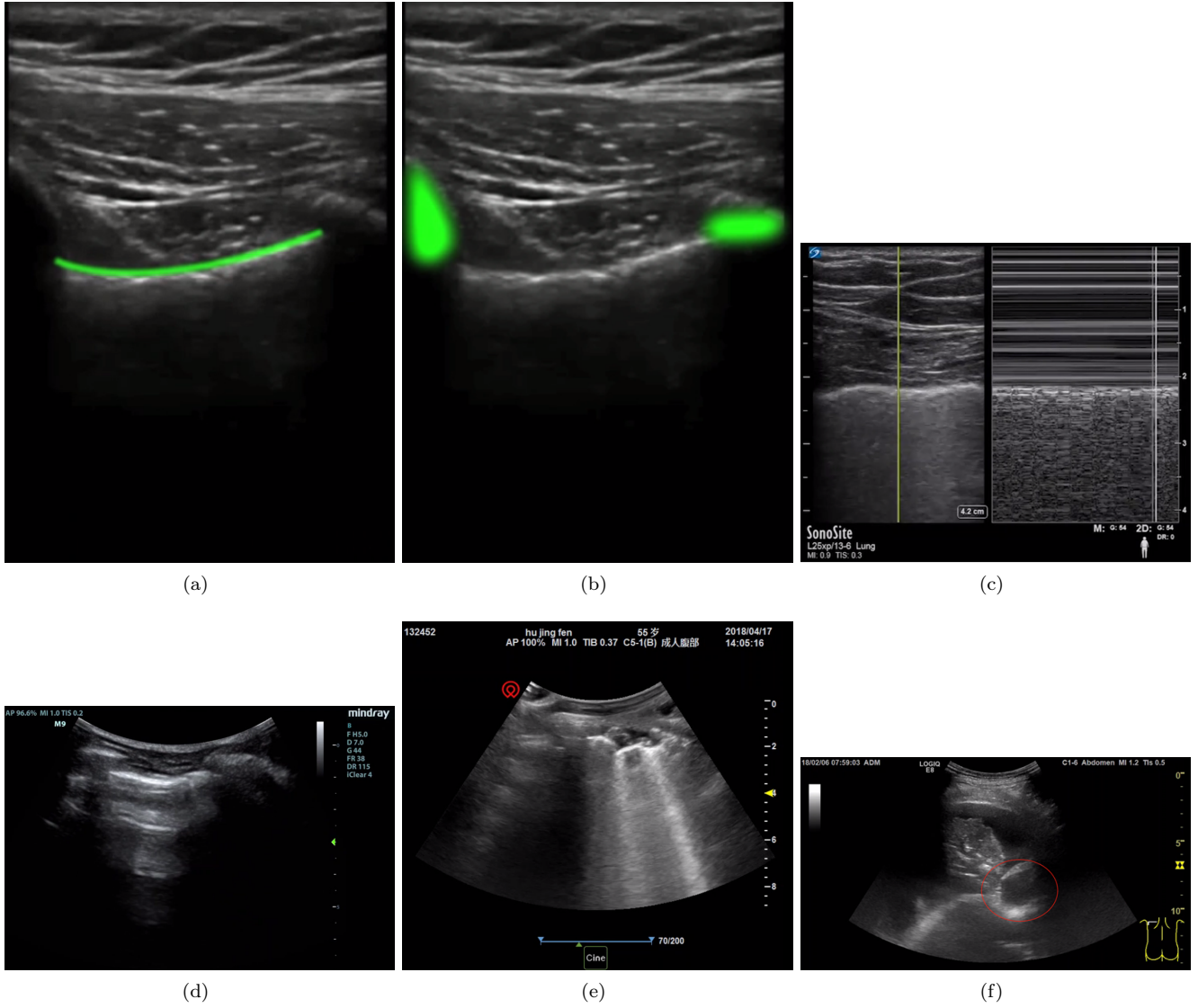


FIG. 1. Example images for various types of Lung signs.²⁰ (a) Pleural line, (b) Bat sign, (c) Seashore sign, (d) A-line, (e) B-line, (f) Atelectasis.

(6) **Lung cancer:** In the case of a peripheral lung tumor, LUS can clearly show the chest wall with the solid lung tissue as the “sound window”. US can clearly captures the chest wall, pleura and peripheral lung lesions, and can show the morphology, boundary and blood flow of the lesions and the anatomical relationship between fine structures and the surrounding tissue, which provides basic information for clinical diagnosis.²⁰ Through their US morphologies, one can distinguish benign and malignant lung tumors.

(7) **Congenital diaphragmatic hernia (CDH):** A recent study³² has found that the LUS patterns for CDH diagnosis include *i.* partial absence of the hyperechoic line representing the normal diaphragmatic profile, *ii.* partial absence of the pleural line in the affected hemithorax, *iii.* absence of A lines in the affected area, *iv.* presence of multi-layered area with hyperechoic contents in motion (normal gut), and *v.* possible presence of parenchymatous organs inside the thorax (i.e., liver or spleen).

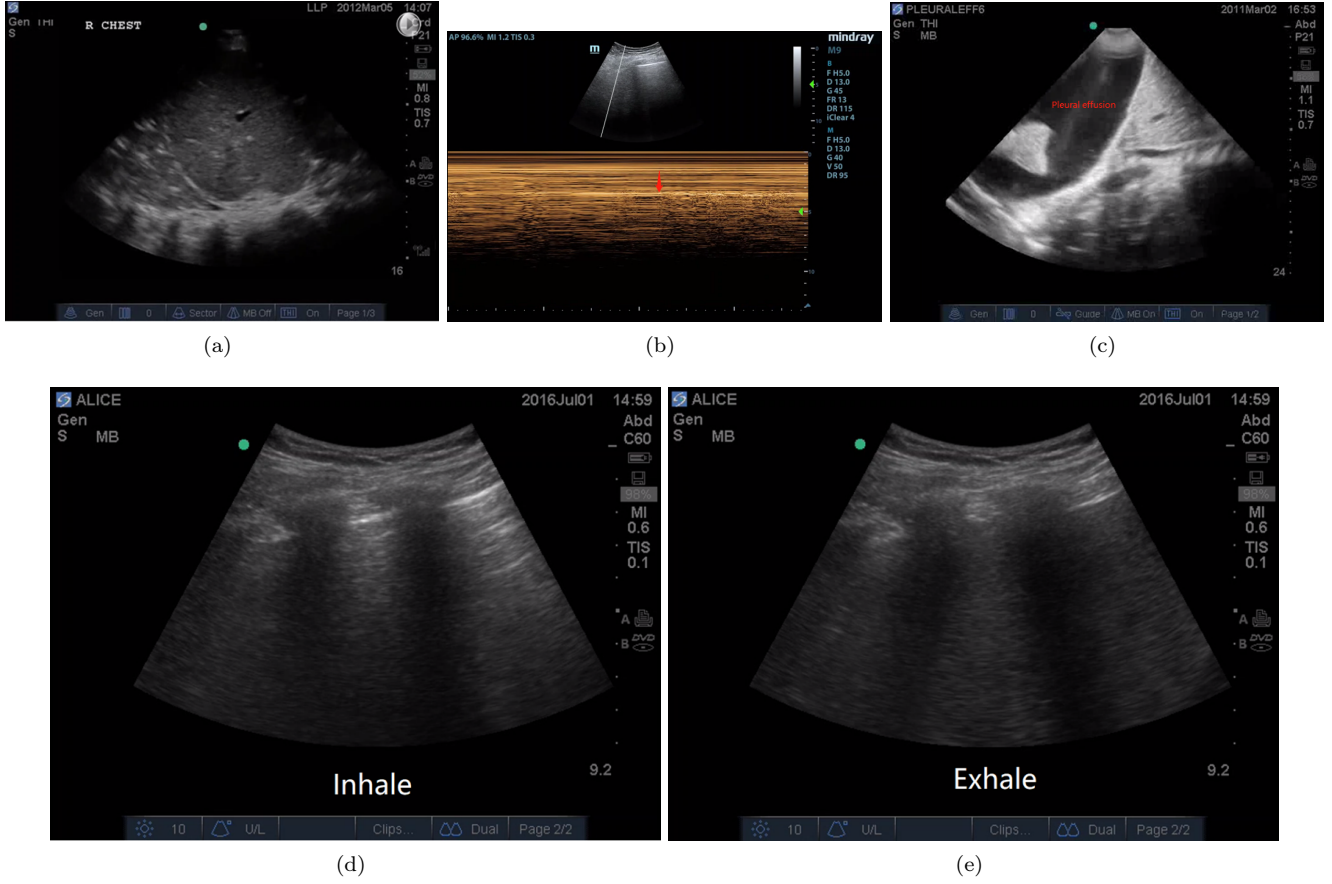


FIG. 2. Example images for various types of Lung signs.²⁰ (a) Bronchial inflation, (b) Lung point, (c) Pleural effusion, (d) and (e) Curtain sign.

In addition to the above conditions, LUS is also invaluable for the analysis and evaluation of lung related children diseases and in intensive care unit (ICU) applications.

- **ICU uses of LUS:** A study from 2016¹ confirmed that the diagnostic efficacy of LUS in some lung and pleural diseases for critically ill or mechanically ventilated patients is equivalent to that of chest CT and better than that of X-ray. For example, LUS can effectively detect lung consolidations with a thickness greater than 20 mm in ICU patients, reaching an overall sensitivity of 90% and a specificity of 98%. Another factor is that the incidence of pleural effusion in ICU patients is very high. About 41% of patients suffer from pleural effusion when they are transferred to the ICU, and

62% of patients may develop pleural effusion during ICU hospitalization³³. Around 19% of mechanically ventilated patients are diagnosed with ARDS and an increase in extravascular lung water is observed. The diagnosis and monitoring of these diseases can be done with LUS, thereby evaluating the respiratory system and circulatory system in real time.

- **Paediatrics:** As a radiation-free imaging modality, ultrasonography is especially suitable for sensitive people such as children, especially for newborns whose musculoskeletal system is not fully developed and whose lung air content is low. LUS has high diagnostic sensitivity and specificity for pediatric lung diseases such as: Neonatal respiratory distress syndrome (NRDS), meconium aspiration syndrome, acute pneumothorax,

occult atelectasis, etc. It has already replaced X-ray diagnosis in neonatal intensive care units as the first choice for the diagnosis of lung diseases.

IV. LUS IMAGE PROCESSING AND ANALYSIS

This section presents the latest advances in image processing methods for LUS. The methods are grouped into two broad categories, specifically into the more standard **model-based** approaches and the **data-driven** (or learning-based) methods.

A. Model-Based Methods

In order to accurately identify the various signs of disease in LUS images, the reconstruction of high quality images through observations and the extraction of information therein are necessary. This is commonly posed as an inverse problem. The solution however may not be unique, or it may be highly sensitive to changes in the data, which illustrates the ill-posedness of the problem. The traditional methods convert this into a well-posed one by using regularization/penalty functions or prior information. Normally, the regularization term is related to the prior information of the parameter to be estimated¹⁵. In the relevant literature, there are three main categories of approaches, which include (i) statistical methods, (ii) regularized geometric modeling methods and (iii) methods based on sparse representations³⁴ or, sometimes, a combination thereof. In the following, we discuss the most widely studied inverse problems in conjunction with medical US image processing, which are also relevant to LUS. Approaches peculiar to LUS specifically are discussed in [IV A 4](#).

1. Despeckling

Generally, the final envelope detected US image is composed of two elements, the useful signal component (corresponding to structure inside the human body) and

the noise component (comprising multiplicative speckle and additive measurement noise).

$$f(x, y) = g(x, y)n(x, y) + w(x, y), \quad (x, y) \in Z^2 \quad (2)$$

where $n(x, y)$ and $w(x, y)$ represent the multiplicative and additive noise components, respectively. (x, y) are the two-dimensional spatial coordinates; $g(x, y)$ and $f(x, y)$ represent the speckle free and the observed signals, respectively. Since the influence of the additive noise is far less obvious than that of the multiplicative noise, the image formation model (2) can usually be approximated by

$$f(x, y) = g(x, y)n(x, y), \quad \text{where } (x, y) \in Z^2. \quad (3)$$

The term $n(x, y)$ corresponds to speckle noise, which is an inherent phenomenon in US images, as well as in other coherent imaging modalities such as the synthetic aperture radar (SAR) or laser imaging. Speckle noise has been shown to be correlated with the tissue structure, so its statistical description generally depends on the type of tissue and the imaging system. It exhibits granular patterns, which obscure fine anatomical details, and thereby reduce the diagnostic accuracy. Speckle noise is hence regarded as an undesirable phenomenon in most clinical applications. There are situations however, when speckle noise can constitute useful information, such as when used for speckle tracking (i.e. motion estimation) and tissue characterization¹⁵. To mitigate speckle, a logarithmic transformation is usually employed to convert the multiplicative characteristics into an additive model.

In the computational US imaging literature, several techniques have been developed for reducing speckle noise. Achim et al.³⁵ use the heavy-tailed α -stable family of distributions to describe US image subbands in a transform domain, to capture the significant non-Gaussian behaviour. Based on this statistical characterisation,

they develop a blind speckle-suppression processor, which non-linear characteristics related to the degree of non-Gaussianity of the data.

Duarte-Salazar et al.³⁶ thoroughly describe 27 techniques that can be utilized to smooth or eliminate speckle noise in medical US images. These technologies can be divided into five categories: (1) dynamic analysis, (2) time-frequency analysis, (3) modern technology, (4) hybrid technology, and (5) machine learning. The majority of the algorithms can eliminate speckle noise but neglect the preservation of details. Therefore, in order to simultaneously fulfill the need for excellent speckle noise removal and edge information preservation, Garg and Khandelwal³⁷ propose a method based on the modeling of the shear wave coefficients of the ultrasonic image detail band after logarithmic transformation. In each detail shearlet subband, the coefficients corresponding to the signal and speckle noise are modeled as normal inverse Gaussian and Gaussian priors, respectively. Based on the local statistics of the image, these coefficients are categorized into homogeneous regions, heterogeneous regions and strongly heterogeneous regions. Then, with the prior distribution, maximum a posteriori estimation (MAP) is performed on all regions of the detail bands, except the strongly heterogeneous regions. An adaptive weight function is also used in the MAP expression to reduce the loss of feature information.

Choi and Jeong³⁸ employ various approaches such as the speckle reduction anisotropic diffusion (SRAD) filter³⁹, discrete wavelet transform (DWT) using symmetric characteristics, gradient domain guided image filtering (GDGIF) and weighted guided image filtering (WGIF). Under the multiplicative noise assumption, SRAD filtering can be used directly to suppress speckle noise, because it does not require log-compression. Moreover, eliminating the additive noise (additive white Gaussian noise) in the wavelet domain is straightforward.

Therefore, the multiplicative noise in the SRAD composite image is converted into additive noise through a homomorphic transformation. Following the application of two-level DWT decomposition, in order to suppress the residual noise of an SRAD filtered image, GDGIF and WGIF are exploited to reduce noise from seven high-frequency sub-band images and one low-frequency sub-band image, respectively. Finally, a speckle-free image is attained through inverse DWT and an exponential transformation.

Chen et al.⁴⁰ suggest a technique for removing speckle noise, where the energy minimization model is solved by the alternating direction multiplier (ADMM) algorithm⁴¹. The convexity, existence and uniqueness of the solution of the new energy minimization model are furthermore proved. It effectively reduces the speckle and achieves considerable performance in terms of visual evaluation and quantitative measurements.

2. Deconvolution

Another important type of model-based US methods is image deconvolution, whereby US images are modeled as a convolution between a blurring kernel or PSF, and the tissue reflectivity function. The linear image formation model can be rewritten as

$$y(r) = h(r) \otimes x(r) + n(r), \quad r \in R, \quad (4)$$

where $y(r)$ is the image pixel observed at position r , $x(r)$ is the TRF to be estimated, $h(r)$ is the system PSF, $n(r)$ is the additive measurement noise. R refers to the image domain¹⁵.

Deconvolution in medical imaging is commonly employed to improve visual quality for and achieve better contrast. This translates in easier interpretation for the physicians. Standard deconvolution schemes exploit simplified models for the tissue reflectivity, prevalently Gaus-

sian or Laplacian, which are typically chosen to produce the most visually pleasing images. The statistics of the restored solutions are hence badly biased by these prior assumptions, and are not always well suited for further information extraction⁴².

Among the completely blind deconvolution strategies, predictive deconvolution⁴³ represents an important solution, but very few authors spent considerable efforts in this direction. Their drawback relate to the simplistic assumptions made in order to fit various real complex scenarios⁴². The most common strategy is instead to exploit different approaches, relying upon statistical estimation and convex optimization theory.

Zhao et al.⁴⁴ study a blind deconvolution algorithm for ultrasound images in a predictive deconvolution manner, where they model the ultrasonic PSF based on a Gaussian function modulated by a sinusoid. Given this parametric model, the estimation of the power spectrum requires estimation of its parameters. In addition, an ℓ_p -norm ($0 \leq p \leq 2$) regularization term of the US TRF is employed, based on the assumption that the US images follow a generalized Gaussian (GG) distribution. An alternate optimization method based on the block-coordinate descent framework⁴⁵ is proposed to estimate US PSF and TRF. Due to the parametric nature of the PSF model, instead of estimating all the PSF pixels, only a few parameters need to be estimated. This reduces the computational load and estimation complexity.

Unlike the predictive deconvolution, MAP-based deconvolution tackles the problem using a two-step scheme: the PSF is estimated first and subsequently image restoration is performed. These techniques represent the most common strategies for medical US image restoration. Their main advantages are *i.* two dimensional or even three dimensional PSFs can be accounted for, *ii.* no assumption is made on the PSF, neither on the number of zeros or poles, and nor on the position of the zeros

on the complex plane, and *iii.* more advanced models than white Gaussian can be assumed for the tissue reflectivity⁴². Although commonly employed, MAP deconvolution brings an increased computational cost, even if simple schemes are employed such as based on Wiener filtering or ℓ_1 -norm optimization. Another problem is that the PSF estimation is still tedious. In particular this is due to the need for phase unwrapping procedures where non-minimum phase PSFs are considered.

Due to the inherent bandwidth limitations of US scanners and the adverse effects of measurement noise, image deconvolution is very sensitive to errors occurring in the PSF estimation. Even slight errors in the PSF estimates can lead to obvious artefacts that render the reconstructed images worthless. To address this, Michailovich et al.⁴⁶ propose a “hybrid” deconvolution technique. Their method is based only on partial information about the PSF, especially its power spectrum to estimate tissue reflectivity. While directly estimating the reflectance of the tissue from the relevant radio-frequency (RF) data, the proposed approach simultaneously eliminates errors caused by inaccuracies in PSF estimation.

Pham et al.⁴⁷ propose a novel algorithm for the retrieval of blood flow from a sequence of ultrafast US images, based on the combination of two different techniques: deconvolution robust principal component analysis (DRPCA) and blind deconvolution (BD). The proposed method overcomes the main limitation of the former related to the requirement for PSF estimation, whilst providing similar performances. The PSF is however assumed to be spatial-temporally invariant, and the algorithm appears computational complex.

3. Segmentation

Classical approaches for image segmentation are formulated in either a Bayesian or a variational framework. The literature spans three widely adopted types

of segmentation approaches, which include (1) thresholding methods, (2) edge-based methods and (3) region-based methods. Since US images suffer from low signal quality caused by the attenuation, speckle, and shadows, many methods often utilize specific constraints or priors. Some widely used constraints are intensity-based priors, geometric priors, and statistical priors. The various US segmentation methods embed these constraints into Bayesian methods, active contours, active appearance models, level-sets, clustering, or graph-based frameworks¹⁵.

Talebi et al.⁴⁸ propose a segmentation method combining genetic algorithms and active contours. This has been proved to overcome some limitations of classical active contours, such as contour initialization and the entrapment of the contour in local minima caused by the existence of speckle noise. But the limitation of Talebi et al.⁴⁸ method is that it can only correctly segment circular tissue in US images.

Luo et al.⁴⁹ combine region and edge information into a robust graph-based segmentation method. The corresponding optimization problem is formulated as a multi-objective problem. They maximize the difference between the target and the background, improve the uniformity in the target area, and consider the edge gradient. The algorithm has several prerequisites. First, the operator should be well experienced. Second, the tumor centered image (TCI) should be carefully delineated to capture the full lesion region with partial surrounding tissues. Third, the region of interest (ROI) around the lesion must be centrally located and the user's participation is necessary. Besides, the algorithm is computationally expensive.

4. Model-based LUS Image Processing

Most ultrasound image processing approaches specifically developed for LUS focus on the identification of line

artefacts. For instance, Ramin et al.⁸ aim to automatically detect B-lines. They characterize the distribution of B-lines in conjunction with their ability to discriminate between healthy volunteers and patients with pulmonary edema. They use a random walk method to delineate the pleural line, and then exclude the upper pleural region before identifying B-lines. This is achieved by an alternate sequential filtration, and subsequently they apply the top-hat filter to ensure that B-lines are laterally detached. Finally, a Gaussian model is fitted to each detected B-line, and the peak point of the fitted Gaussian models corresponding to the B-lines are calculated and used to accurately determine the position of B-lines. B-lines are then overlaid on the B-mode images.

Brusasco et al.⁵⁰ endeavor to develop a fully automatic method of quantifying B-lines and thereby determining extra-vascular lung water (EVLW). B-lines are selected from the input gray-scale LUS images and confirmed when white pixels take up at least 50% along the image columns and over 70% of the total vertical length of the image. B-lines quantification is realized by performing a statistical regression on the segmented LUS images. Although this study provides a reliable operator-independent assessment of EVLW, this method may fail when multiple B-lines coalesce into a single white line rather than close-by B-lines.

Anantrasirichai et al.⁵¹ propose an innovative way of detecting line artefacts in LUS images by solving an inverse problem. The method combines the Radon transform with the PSF of the US acquisition system in a single equation thereby achieving line detection and deconvolution simultaneously. This inverse problem is solved using the ADMM algorithm, offering a fast convergence rate. The scheme firstly detects the pleural line in order to locate the lung space. Then, the local peaks of the Radon transform are detected and line-type classification is done following clinical definitions, in the spatial

image domain. B-lines, A-lines and Z-lines are hence successfully identified. To enhance line detection performance and the visualization of restored lines, they include an additional convolution factor in the Radon transform domain with an unknown blurring kernel. The penalty function employed is ℓ_p -norm with low values of ($0 \leq p \leq 1$) in order to promote sparsity in the Radon space.

Extending the above work in the context of evaluating COVID-19 patients, Karakus et al.⁵² further improve the line detection performance by regularizing the solution using the Cauchy proximal splitting (CPS) algorithm⁵³. The key benefit of this type of work is that it offers an unsupervised framework for the detection of B-lines in situations where annotated data are not freely available. These methods converge rapidly, enabling thus the processing of LUS image sequences in a relatively short amount of time with high detection accuracy.

Table I summarizes the algorithms presented in this section and their effectiveness in various applications.

B. Data-Driven Methods

Compared to conventional signal processing methods, ML based methods can provide improved performance in medical imaging, because they are able to capture more complex patterns in the data. ML is referred to as being data-driven as large amounts of data are generally required for training and testing. One of the branches of ML is deep learning, a class of techniques that have characteristic three important properties⁵⁴: **i.** features are learned from the data instead of being hand-crafted, **ii.** features are abstracted in a hierarchical way from lower level to higher level, and **iii.** the number of non-linear feature transformation layers is at least two.

Over the past few years, DL techniques have rapidly gained attention in the field of medical imaging applications, their applications ranging from image analysis and

interpretation to image formation and reconstruction⁵⁵. The key to image reconstruction is to find a good sparse representation of the image to be reconstructed (which is also true for model-based approaches). DL methods assume that the representation is provided by deep neural networks, so it is nonlinear. The model parameters of the representation must be learned from a large amount of data. Supervised learning is the most popular method since it can lead to highly accurate solutions. The design of the network is flexible but generally has a relatively high complexity. Stochastic optimization strategies, can effectively extract data features from low-level to semantic level. Representative methods include deep image prior (DIP) and generative adversarial networks (GAN)^{56,57}. Due to these advantages, data driven methods have shown a great potential in various automated US image analysis tasks.

A review by Liu et al.⁵⁸ describes several popular DL architectures, including *i.* supervised deep networks or deep discriminative models, *ii.* unsupervised deep networks or deep generative models, and *iii.* hybrid deep networks. The authors point out that the current basic models used in medical US analysis are mainly convolutional neural networks (CNNs), recurrent neural networks (RNNs), deep belief networks (DBNs), autoencoders (AEs), and variants thereof. They summarized and discussed the application of these models in detail for various specific tasks in US image analysis. These include *i)* traditional diagnostic tasks, such as classification, segmentation, detection, registration, biometrics, quality assessment, and *ii)* emerging tasks like image-guided interventions and treatments. They state that the main problem is the small sample datasets generally available. The common workaround is to perform transfer learning, which can be either cross-domain or cross-modal. The former is the most common way to accomplish a variety of tasks in medical US analysis, but

TABLE I. Summary of Model-Based Methods

Application	Algorithm	Details	Data	Effectiveness	Reference
De-speckling	Multiscale Bayesian speckle suppressing algorithm	The wavelet transform based on subband representation function; and a Bayesian denoising algorithm based on an alpha-stable prior for the signal	44 abdominal US images from the same patient and DICOM image files donated by various vendors	The method has a good adaptation ability for biomedical images denoising when the noise can be modeled as additive Gaussian and signal-independent.	Achim et al. ³⁵
	GDGIF and WGIF	GDGIF and WGIF are applied to the discrete wavelet transformed data that comes from SRAD filtered images	6 standard images and 6 real US images of aligant breast lesions	Higher PSNR and better feature conservation ability than conventional methods. Low computational cost in standard images(9.9913%) and US images(2.7186%)	Choi and Jeong ³⁸
	ADMM	Minimization of a convex energy model - an adaptive total variation model	synthetic, natural, and real medical ultrasound images.	Highest PSNR and SSIM of the restored images by the different model and visually fewer textures of residual images.	Chen et al. ⁴⁰
	DST-MAP	MAP estimation on the modeled shear wave coefficient based on DST of log-transformed images	Synthetic US images and 60 real US images	Best performance at high noise variance in synthetic US images. Highest mean to variance ratio and equivalent number of looks in all marked regions in real US images.	Garg and Khandelwal ³⁷
Deconvolution	Alternating optimization algorithm	Parameter estimation of the US PSF modeled by Gaussian function modulated by a sinusoidal function	Simulated and in-vivo US images	Visually and quantitatively better than the non-blind method in simulated images. Competitive performance but lower computational load compared with non-blind deconvolution algorithm.	Zhao et al. ⁴⁴
	Alternating minimization	Proximal gradient method(PGM) to estimate the tissue reflectivity function as well as the minimization of the DFT of the PSF	In-vivo RF images acquired from healthy people	Reasonable computational efficiency. Noticeable increase in spatial image resolution and improved contrast. No “ringing” effects or residual blur around sharp image details.	Michailovich et al. ⁴⁶
	BD-RPCA	Iterative estimation of PSF and the blood component based on Casorati matrix, using BD and DRPCA respectively.	Simulated and in-vivo US data	Comparable NRMSE and PSNR with DRPCA in both simulated and in-vivo US images but higher computational cost.	Pham et al. ⁴⁷
Segmentation	Genetic algorithm	Genetic active contour with an energy minimization procedure.	US images with circular tissue structure	Satisfactory segmentation results but time consuming.	Talebi et al. ⁴⁸
	Multi-objectively optimized robust graph-based (MOORGB) segmentation method and Partial swarm optimization (PSO) algorithm	A multiobjective optimization function which combines region-based and edge-based information is designed in the PSO to optimize the RGB.	100 clinical breast US images and 18 clinical musculoskeletal US images	Low averaged radial error(ARE) at 10.77% and good overall performance in TPVF(volume fraction) , FPVF and FNVF.	Luo et al. ⁴⁹
Detection	Alternate sequential filtering and top-hat filtering	After removing the pleural line detected by a random walk method, B-lines are identified using ASF and white top hat filtering, and finally enhanced by Gaussian model.	US images from 4 healthy subjects and four patients with pulmonary edema.	Successfully differentiate between the healthy and unhealthy class with a p-value of 0.015. Average number of B-lines of patients and healthy group are 0.28 ± 0.06 and 0.03 ± 0.06 respectively.	Ramin et al. ⁸
	simple linear regression (SLR) and robust linear regression (RLR)	B-lines are selected through contrast adjustment, K-means classification, ASF, and confirmation. Statistical regression is used for quantification.	12 patients with acute respiratory distress and each provided with 12 LUS frames.	Provides a reliable operator-independent assessment of EVLW in ARDS, which is comparable or superior to previous scores.	Brusasco et al. ⁵⁰
	ADMM	Radon transform based non-convex optimization with the combination of the PSF function.	50 simulated images and in-vivo US B-mode images	Improves the performance of B-line detection approaches by up to 50%.	Anantrasirichai et al. ⁵¹
	Cauchy Proximal Splitting (CPS)	Radon transform based non-convex optimization with Cauchy-based penalty function	12-segment LUS for 9 COVID-19 patients	Up to 88% detection accuracy	Karakus et al. ⁵²

its source and destination are not within the same domain. However, the solution to train models on natural images might not be the optimal one and therefore domain-specific models in medical imaging are normally

considered to enhance performance. In this sense, cross-modal transfer learning may be a wiser choice.

Razzak et al.⁵⁹ also discuss the application of ML and DL in US, outlining the main challenges and solutions. They highlight the importance of future ML sys-

tems to provide real-time feedback to the sonographer during image acquisition. It will also be important to replace manual ROI selection with automatic ROI selection or at least with a hybrid solution involving the human in the loop.

1. Deep learning and inverse problems

A review on the use of DL methods to solve inverse problems in imaging in general is provided in Lucas et al.⁶⁰. Some popular neural network architectures used for imaging tasks are recalled, such as the classic multilayer perceptron, autoencoder-based architectures and U-Net with skip connections. The questions as to why and how these DL tools can solve specific inverse problem are answered. Although not specifically focused on medical ultrasound, most of the finding reported in this review are relevant and can inspire the development of DL techniques in LUS.

There are obvious theoretical connections between DL networks and traditional iterative algorithms. Jin et al.⁶¹ explore the relationship between CNNs and iterative optimization methods for a special type of inverse problem. Observing that the operator involved in the forward model corresponds to a convolution, they propose a method that combines a fast, approximate solver with CNNs to solve inverse problems. The proposed method, which is called FBPCovNet, combines filtered back projection (FBP) with a multiresolution CNN. The structure of the CNN is based on U-Net⁶², with the addition of residual learning. This approach is motivated by the convolutional structure of several inverse problems in biomedical imaging, including CT, MRI, and diffraction tomography (DT).

Despite their superior performance, these specially-trained solvers require retraining to solve other problems. Chang et al.⁶³ propose a general framework to train a single deep neural network that solves arbitrary linear

inverse problems. They observe that in optimization algorithms for linear inverse problems, signal priors usually appear in the form of proximal operators. Thus, the proposed network acts as a proximal operator for an optimization algorithm and projects similar image signals onto the set of natural images defined by the decision boundary of a classifier. The learned projection operator combines the high flexibility of deep neural nets with the wide applicability of traditional signal priors. This has the potential to lowers significantly the costs involved in the design of specialized hardware and medical US is a clear potential beneficiary.

The training of deep networks usually requires a large collection of source-observation pairs, which can be prohibitively expensive and impossible to ensure in medical imaging. To cope with this problem, Tamir et al.⁶⁴ propose to jointly learn the prior and reconstruct images using known noise statistics without access to ground-truth data. They take advantage of (known) noise statistics for each training example and formulate the problem as an extension of basis pursuit denoising with a deep CNN prior in place of image sparsity. When it comes to unsupervised learning however, reconstruction errors increase, which highlights the importance of a large number of training datasets to offset the missing ground-truth information. The choice of measurement loss function and data signal-to-noise ratio also have a significant impact on the quality of reconstruction.

Similarly, without the requirement of any training data, deep image priors methods⁶⁵ have been proposed and showed good performance in various image processing tasks, by capturing low-level image statistics with a generator-like network architecture. Sun and Bouman⁶⁶ proposed a variational inference approach called Deep Probabilistic Imaging (DPI), which uses an invertible flow-based generative model to represent the posterior probability distribution. In both convex and non-convex

inverse imaging problems, this approach enables uncertainty quantification and multi-modal solution characterization.

GANs are also used for image reconstruction⁶⁷ by utilizing pre-trained generative models to approximate the observed data Y . A GAN that models $P(X)$ can naturally act as a good prior for the true source X , thus eliminating the need to choose a prior that can regularize the problem while also being tractable for optimization. Using a pre-trained GAN in the space of source signals, one can reliably recover solutions to under-determined problems in a ‘blind’ fashion, i.e., without knowledge of the measurement process. For example, Marinescu et al.⁶⁸ leverage StyleGAN2, for building powerful image priors. Bayesian reconstruction through generative models combined with different forward operator models are applied in image super-resolution and in-painting tasks, using a single pre-trained generator. However, although these methods were shown to be successful in generic image processing, their practical applicability to LUS is yet to be verified.

2. Despeckling

Deep learning methods can play a compelling role in improving the quality of US images, in terms of speckle mitigation in particular. Such data-driven systems can indeed be leveraged across the US imaging domain⁶⁹. Vedula et al.⁷⁰ proved the applicability of CNNs as a method to quickly and accurately perform image restoration and produced very good results via advanced despeckling algorithms. A multi-resolution fully convolutional neural network (FCN) is used to approximate an ultrasound image of “CT quality”. This end-to-end ultrasonic image despeckling CNN structure effectively improves the image resolution and contrast, and at the same time has a fast computation speed, making it applicable in real-time settings. However, in practice, CT-US paired

data is difficult to obtain, which reduces the applicability of the method. The method proposed by Feng et al.⁷¹ was shown to retain all relevant anatomical and pathological information in the restored images. They introduce a new CNN architecture, called US-Net, and propose a new hybrid loss that contains two parts. One is designed for speckle noise removal, the other consists of error summation of the structural similarity index with respect to the denoised image and original image.

Li et al.⁷² extended a DL algorithm for ultrasonic speckle reduction from 2D to 3D. For the first time, a 3D dense U-net model was proposed to process 3D US B-mode data from clinical US systems. Apart from achieving a suppression and mean preservation index similar to that of traditional denoising, the running time was also reduced by two orders of magnitude.

3. Deconvolution

Deep neural networks have also found applications in ultrasound image restoration. Perdios et al.⁷³ propose to exploit stacked denoising autoencoders (SDA), and successfully applied them to the recovery of structured signals, including US images. They explore both a linear measurement case where a known Gaussian random matrix is used as the measurement matrix (SDA-CNL) and a non-linear measurement case where the weight matrices and bias vectors are learned (SDA-CL). It is shown that a 4-layer SDA-CL outperforms a state-of-the-art compressed sensing algorithm without the need to tune any hyper-parameter. While increasing the quality of the reconstructed image is the main objective, reducing the calculation time is also an important requirement in applications. Yoon and Ye⁷⁴ propose a novel DL approach that interpolates the missing RF data by utilizing the sparsity of the RF data in the Fourier domain. The algorithm effectively reduces the data rate without sacrificing the image quality and is also widely applicable. The

CNN can be trained using a RF data measured by the linear array transducer for a particular organ, and can be extended for other types of transducers and/or different body parts.

4. Segmentation

Current US image segmentation methods often exhibit the following problems: *i)* most segmentation algorithms cannot automatically segment the target area completely and accurately, and manual assistance is required to complete the image segmentation. *ii)* the current algorithms cannot make good use of the inherent characteristics of US images. Due to the complex structure of the human body, the use of some background medical knowledge is necessary to help segmentation of the target contour. *iii.* standard US segmentation methods cannot accurately segment the target area, whilst the segmentation speed is slow⁷⁵.

Lei et al.⁷⁶ focus on the applications of supervised learning methods and weakly supervised learning methods in medical image segmentation. Network architectures based on supervised learning are reported, including U-Net, 3D Net, RNN, Skip connection and cascade 2D and 3D models. Although supervised learning shows strong adaptability to medical image segmentation, the segmentation results rely heavily on high-quality labels. To tackle this problem, weakly supervised learning is studied, and the main methods include data augmentation (traditional augmentation⁷⁷ and synthetic augmentation⁷⁸), transfer learning (pre-trained model⁷⁹ and domain adaptation⁸⁰) as well as interactive segmentation (DeepIGeoS⁸¹, BIFSeg⁸² and GM Interactin⁸³). An unsupervised method is proposed by Chen and Frey⁸⁴. The described ConvNet model minimizes an active contour without edges (ACWE)-based energy function, which depends only on the intensity statistics of the given image. An image training set is

used to optimize CovNet parameters. The network learns a universal representation that can segment images not seen previously, based on their intensity statistics. In the presence of ground truth data, the available segmentation labels are utilized to incorporate structural information during network training. Wang et al.⁸⁵ provides a comparison of medical US image segmentation results using major DL-based segmentation algorithms.

5. Data-Driven LUS Image Processing

The data-driven algorithms described in the previous sections work effectively in medical ultrasound image processing, and they have already started to make an impact in LUS image analysis in particular. McDermott et al.⁸⁶ has demonstrated the applicability of LUS imaging to COVID-19 diagnosis.

As a first example, Correa et al.¹¹ combine image processing and vector classifiers for the diagnosis of consolidations of pediatric pneumonia. The pleural line is first identified, and skin/soft tissue removal is then carried out. Based on brightness profiles, features can be extracted. A standard neural network is trained to implement the above process and is able to correctly identify pneumonia infiltrates. However, only severe and radiographically evident cases are analyzed in this study; this may imply reduced performance of the algorithm in less severe cases, where a lower sensitivity is expected. Besides, vectors distributed in the training/testing set, corresponded to a single patient so the model could be overfit, and the algorithm requires validation for individual ultra-sonographers.

Different network architectures were explored in the literature. The approach introduced by Kulhare et al.⁸⁷ automatically segment LUS features in simulated animal models with single shot neural nets. However, the success of application to human LUS images has not been investigated. Due to the reduced availability of LUS image

datasets and of corresponding high-quality labels, the use of semi-supervised learning and unsupervised learning is becoming a trend. Sloun and Demi⁸⁸ explore weakly-supervised DL techniques, requiring only a single label per frame for training, and that has been applied and tested both in-vitro and in-vivo. Notably, the proposed method enables B-line detection in real-time, and can also serve as a region-of-interest selector for further quantitative analysis of segments in the US data that contain the most relevant information.

Artefact quantification has always been considered the primary aim of clinical applications of LUS, since it plays a significant role in clinical diagnosis. Wang et al.⁸⁹ attempt to perform real-time lung comet quantification through ML to diagnose and quantify pulmonary edema. This neural network is constructed by considering a input with relatively high resolution and a training dataset of small size. Rectified linear units (ReLU) are chosen as the activation functions for the neurons due to a reported faster training speed and the ability to prevent overfitting. The limitation lies in that the size of the database is small, and the database was labeled by a single observer. Considering the wide usage of U-Net in biomedical imaging, this work can potentially be further extended.

Motivated by the COVID-19 pandemic, researchers have been enthusiastically investigating various solutions to increase the speed of diagnosis, and relax the pressure on the health systems all around the world. A recent study proposed by Almeida et al.⁹⁰ was the first to use ML to identify semiological indications of COVID-19 in LUS images. They propose the use of MobileNets (light-weight neural networks) to support diagnostics of COVID-19. (MobileNet was pretrained on ImageNet, substituting the last layer for a fully connected layer with a ReLU activation and the output layer with a softmax activation). Multitask learning is realized by training different MobileNet models for each indication. The

method has various potential applications. For example, MobileNet could be of benefit through the provision of more accurate image interpretation, especially for less experienced operators, and might reduce examination times, which is associated with greater resources and reduced costs for the health care systems. The drawback of this method is the non-specific pretraining on ImageNet dataset. Born et al.⁹¹ explore automatizing COVID-19 detection from LUS imaging in order to speed-up the assessment process. They publish the first dataset of lung POCUS recordings of COVID-19, pneumonia, and healthy patients. The collected data is heterogeneous but was pre-processed manually to remove artifacts and checked by a medical doctor for quality. A model was trained based on a pre-trained convolutional network (POCOVID-Net) on the available data and evaluated using 5-fold cross validation. Once more data becomes available, improvements to POCOD-Net should be considered. This could be achieved by pre-training the model on (non-lung) US samples instead of using a database of real-life objects, for instance ImageNet. This pre-training may help detecting specific patterns in LUS image such as B-Lines. Generative models could help complement the scarcely available COVID-19 data.

Roy et al.⁹² propose an extended and fully-annotated version of the ICLUS-DB database⁹³. They present a novel deep network, derived from spatial transformer networks⁹⁴, which simultaneously predicts the disease severity score associated to an input frame and provides localization of pathological artefacts in a weakly-supervised way. A new method is also introduced based on uninorms for effective frame score aggregation at a video-level. This research paves the way to future research on DL for the assisted diagnosis of COVID-19 from LUS data.

In order to fully exploit line artefacts in LUS images, Carrer et al.¹⁰ and Baloesu et al.⁹⁵ track the ap-

pearance of pleural lines and B-lines respectively. Carrer et al.¹⁰ propose an automatic and unsupervised method for the detection and localization of the pleural line in LUS data based on a hidden Markov model and Viterbi algorithm. The pleural line localization step is followed by a supervised classification procedure based on support vector machines (SVM), then a classifier evaluates the healthiness level of the patient. The performance on the dataset obtained with convex probes was found to be slightly poorer than that from linear probes. Baloesescu et al.⁹⁵ propose the largest study to date on automated assessment of B-lines. It chooses a relatively shallow custom-made network (CNN) architecture with 3-D filters (called 3-D CsNet) for B-line assessment, for the purpose of distinguishing between the presence and absence of B-lines as well as assessing B-line severity. The proposed algorithm is fast, employing few trainable parameters, it is more flexible and easier to deploy since it alleviates the need for pre-training. It is also effective in poorer quality datasets. Moreover, it uses a severity metric based on expert judgment rather than the number of B-lines, producing accurate results. Nevertheless, there are still various issues with this approach. Specifically, the learning data comes from only one brand and type of US device, not from different probe types, and the unequal proportion of clips in each severity category may influence the classification performance. It also exhibits weaker performance on multiclass severity rating, potentially due to the presence of a high number of categories, which may determine inaccurate decisions of the DL method.

Similar to Carrer et al.¹⁰, Veeramani and Muthusamy⁹⁶ use two relevance vector machines (RVM) to detect abnormalities in LUS images. Specifically, the binary RVM decides whether the given input LUS image corresponds to a healthy or unhealthy subject. If abnormal, the images will then be classified by the multi-level

RVM into one of the given lung diseases, including respiratory distress syndrome, transient tachypnea of the new born, meconium aspiration syndrome, pneumothorax, bronchiolitis, pneumonia, or lung cancer. The classification accuracy achieved by the multi-level RVM is higher than 90%.

The alternative solution of employing transfer learning, in particular in small dataset has also been explored. Horry et al.⁹⁷ compare the performance of 8 widespread network structures, which are amenable to transfer learning, for COVID-19 diagnosis for 3 modalities, including X-ray, CT and US. Overall, the results show that DL models perform extremely well on the LUS image dataset, with VGG19 in particular outperforming all other models. The work not only uncovers the challenging aspect of the limited availability of COVID-19 image datasets, but also describes a pre-processing pipeline to remove sampling bias and improve image quality.

Table II provides a succinct description of all the aforementioned data driven methods.

V. DISCUSSION

Clinical applications of LUS are more and more numerous. They include, among others, emergency departments and intensive care units, making LUS an increasingly popular application of medical ultrasonography. LUS is a non-invasive, economical, real-time imaging modality, without radiation hazards or complications, and easily available at the bedside. All these features help LUS reduce the need for chest X-ray or CT scans.

As the second largest organ of the human body, the lungs are prone to various diseases. Their condition can be used to monitor various conditions, such as pulmonary edema, pneumonia, and pneumothorax. In clinical practice, many characteristics of the lungs, such as the pleural line, A-lines or B-lines, can be obtained by analyzing LUS images. By monitoring the presence and changes

TABLE II. Summary for Data Driven Methods

Application	Algorithm	Details	Data	Effectiveness	Reference
De-speckling	Multi-Resolution CNN	A multi-resolution fully convolutional neural network consisting of a down-sampling and an up-sampling track.	Cancer Imaging Archive(TCIA)	A speed-up in run-times and an average PSNR of 23.79dB	Vedula et al. ⁷⁰
	US-Net	Adam optimization of a CNN-based model with a hybrid loss function of MSE and SSIM	Synthetic Images and thyroid US Images from Peking University Hospital	Highest PSNR and SSIM on different noise levels.	Feng et al. ⁷¹
	3D U-Net	4-layer encoder-decoder architecture where each layer includes 3D convolutional operations and ReLU activations. Skip connections and dense connections are introduced.	4D US volume sequences of liver scans from 24 healthy volunteers.	Speckle suppression and mean preservation index (SMPI) of 1.092 ± 0.11 on the test dataset	Li et al. ⁷²
Deconvolution	SDA-CNL and SDA-CL	4 fully-connected layers where the first compresses the signals and others for recovery	PICMUS	Considerable PSNR improvement when down sampling ratios below 0.3	Perdios et al. ⁷³
	Deep CNN	CNN performs direct interpolation of RF data and the reconstruction is done using the standard delay-and-sum(DAS) beamformer.	15000 Rx-SC planes of 7 people for generating training data, and 3000 Rx-SC planes of another person for validation dataset	Successfully reconstruct the missing RF data from only 25% of RF data. With the average PSNR of 30.92	Yoon and Ye ⁷⁴
Segmentation	ConvNet	An active contour without edges(ACWE) framework is parameterized via a ConvNet, of which the parameters are optimized using a self-supervised method.	Highly realistic simulated Tc SPECT images	Training with the combination of ACWE loss and label loss brings great improvements.	Chen and Frey ⁸⁴
Detection	Characteristic vector classifiers	Feature extraction based on the analysis of brightness distribution patterns present in rectangular segments from the images.	60 LUS frames corresponding to 21 children under 5.	90.9% sensitivity and 100% specificity for pneumonia infiltrates identification	Correa et al. ¹¹
	Single shot neural nets	Six single-class SSD networks for Image-based lung feature detection	Swine lung pathology models	At least 85% in sensitivity and specificity for all features.	Kulhare et al. ⁸⁷
	CNN	CNN for B-line detection and weakly-supervised localization through class activation mapping.	ULA-OP in-vitro data, ULA-OP in-vivo data and Toshiba in-vivo data	B-line detection rate as high as 91.25% when a specialist uses entire CAM videos.	Sloun and Demi ⁸⁸
	CNN	A basis CNN with data augmentation and dropout to avoid overfitting	4864 clinical US images	An accuracy of 43.4% for counting the number of comets and an intraclass correlation (ICC) of 0.791 with respect to human counting	Wang et al. ⁸⁹
	MobileNets	MobileNet pretrained on ImageNet, substituting the last layer for a fully connected layer with a ReLu activation and the output layer with a SoftMax activation.	12718 COVID-19 images extracted from 60 different LU videos	MobileNet outperforms Zero Rule classifier Compared with junior radiologist, MobileNet improves specificity with a minor loss in sensitivity	Almeida et al. ⁹⁰
	POCOVID-Net	The convolutional part of VGG16 followed by one hidden layer with ReLu activation, dropout of 0.5 and batch normalization followed by the output layer with SoftMax activation.	POCUS dataset	A sensitivity of 0.96, a specificity of 0.79, and F1-score of 0.92 for detecting COVID-19	Born et al. ⁹¹
	Spatial Transformer Networks(STN) based deep network	The concatenation of CNN and STN achieves frame-based score prediction, after which an aggregation is performed for video-based score prediction. Estimation of segmentation masks indicates pathological artifacts in frame-based segmentation.	COVID-19 Images	An F1-score of 65.1 in frame-based score prediction. An F1-score of 61%, a precision of 70% and a recall of 60% in video-based score prediction. A pixel-wise accuracy of 96% and a binary Dice score of 0.75 in segmentation evaluation.	Roy et al. ⁹²
	Hidden Markov model, Viterbi algorithm and SVM	HMM and Viterbi algorithm are used for automatic pleural line detection, followed by feature extraction, after which the SVM-based COVID-19 scoring is carried out.	Italian COVID-19 LUS Dataset (ICLUS-DB)	Average overall accuracy in detecting the pleura is 84% and 94% for convex and linear probes, respectively. The accuracy of the SVM classification in correctly evaluating the severity of COVID-19 is about 88% and 94% for convex and linear probes, respectively.	Carrer et al. ¹⁰
	3D-CsNet	A CNN consisting of eight intermediate layers followed by two fully connected layers. The network is optimized with a cross entropy loss.	B-mode clips from ED patients	A sensitivity of 93% and a specificity of 96% for the presence or absence of B-lines, with a kappa of 0.88	Baloescu et al. ⁹⁵
	multi-level RVM	The binary RVM classifies the pre-processed images as normal or abnormal. If abnormal, the multi-level RVM further determines which lung disease it corresponds to.	Not mentioned	Classification accuracy of above 90% and 100% specificity when compared with SVM and neural networks.	Veeramani and Muthusamy ⁹⁶

of the lung signs, diseases can be accurately diagnosed and evaluated promptly. In particular, B-lines carry a lot of valuable disease information and are often used for facilitating diagnosis.

In order to meet more medical demands, it is often necessary to improve image quality (denoising, deconvolution), and/or extract useful information from the images. The improvement of image segmentation and quantification algorithms can often assist clinical diagnosis. Many of these problems can be posed as inverse ones. The quality of the processed images therefore substantially hinges on the ability to inject accurate prior knowledge into the estimation process. In traditional approaches, inverse problem-solving tasks are usually expressed as optimization problems. Given the observed variables, the signal can be reconstructed by solving the aforementioned optimization problems. The main drawback of the classical methods is that priors are manually selected from a small number of well-performing priors. This limits somewhat the range of prior knowledge that can be employed for reconstruction. ML / DL methods allows useful information to be inferred from low-quality images that are characteristic of US. The use of LUS in conjunction with such data-driven techniques was found valuable in providing faster and more accurate bedside interpretation of LUS.

DL methods such as CNNs have demonstrated considerable performance, often similar to that of humans in a range of image classification tasks. A precise and fast LUS image analysis system based on DL methods could potentially assist clinicians and ease their workload. Various network structures have been put into practice. For example, FCN based on end-to-end learning is a popular segmentation network, among which U-Net is a particularly efficient segmentation algorithm. U-Net and its improved versions have been most widely used in segmentation tasks of different tissues, organs or lesions in med-

ical images. However, these supervised learning methods need a large amount of training data. Small datasets can cause overfitting. Data augmentation and dropouts are two techniques that are typically adopted to address this issue. In fact, datasets with high-quality labels are rarely available, especially in the field of medical image analysis. Because data acquisition and labeling usually incur high costs, most of the datasets are incomplete or imperfect, leading to a gap in US research. Transfer learning is a feasible solution to fill in this gap, for example, a pre-trained network can be first obtained on ImageNet, and then be used for US image training. However the performance is never going to be as good as targeted training on medical image datasets⁵⁸.

The future of computational lung ultrasound imaging most likely consists in combining more and more model-based methods and data-driven approaches for developing unsupervised (or at most semi-supervised) image interpretation techniques that will alleviate the need for labelled training data.

VI. DECLARATION

This manuscript is a preprint and has been submitted for publication in the Journal of the Acoustical Society of America. Please note that, despite having undergone peer-review, the manuscript has yet to be formally accepted for publication. Subsequent versions of this manuscript may have slightly different content.

¹Daniel A Lichtenstein. Lung ultrasound in the critically ill. *Annals of intensive care*, 4(1):1–12, 2014.

²David L. Convissar, Lauren E. Gibson, Lorenzo Berra, Edward A. Bittner, and Marvin G. Chang. Application of lung ultrasound during the covid-19 pandemic: A narrative review. *Anesthesia & Analgesia*, 2019.

³Nathaniel Reisinger and Abhilash Koratala. Lung ultrasound: a valuable tool for the assessment of dialysis patients with COVID-19. *Clinical and Experimental Nephrology*, 24:850–852, 2020.

- ⁴Libertario Demi, Thomas Egan, and Marie Muller. Lung ultrasound imaging, a technical review. *Applied Sciences*, 10(2):462, 2020.
- ⁵BLF.org. Lung disease in the UK, 2021. URL https://statistics.blf.org.uk/?_ga=2.18220605.520238884.1611621128-714148984.1611621128.
- ⁶L. Demi. Lung ultrasound: The future ahead and the lessons learned from covid-19. *The Journal of the Acoustical Society of America*, 148(4):2146–2150, 2020.
- ⁷Ruud JG van Sloun and Libertario Demi. B-line detection and localization by means of deep learning: preliminary in-vitro results. In *International Conference on Image Analysis and Recognition*, pages 418–424. Springer, 2019.
- ⁸Ramin, Moshavegh, Kristoffer Lindskov, Hansen, Hasse, Moller-Sorensen, Michael Bachmann, Nielsen, Jorgen Arendt, and Jensen. Automatic detection of b-lines in in-vivo lung ultrasound. *IEEE Transactions on Ultrasonics, Ferroelectrics, and Frequency Control*, 2018.
- ⁹Liming Hu, Courosh Mehanian, Benjamin K. Wilson, and Xinliang Zheng. Devices, systems, and methods for diagnosis of pulmonary conditions through detection of b-lines in lung sonography, 2019.
- ¹⁰Leonardo Carrer, Elena Donini, Daniele Marinelli, Massimo Zanetti, and Lorenzo Bruzzone. Automatic pleural line extraction and covid-19 scoring from lung ultrasound data. *IEEE Transactions on Ultrasonics Ferroelectrics and Frequency Control*, PP:1–1, 2020.
- ¹¹M Correa, M Zimic, F Barrientos, R Barrientos, A Román-Gonzalez, MJ Pajuelo, C Anticono, H Mayta, A Alva, L Solis-Vasquez, DA Figueroa, MA Chavez, R Lavarello, B Castañeda, VA Paz-Soldán, W Checkley, RH Gilman, and R Oberhelman. Automatic classification of pediatric pneumonia based on lung ultrasound pattern recognition. *PLoS ONE*, 2018.
- ¹²L. J. Brattain, B. A. Telfer, A. S. Liteplo, and V. E. Noble. Automated b-line scoring on thoracic sonography. *Journal of Ultrasound in Medicine*, 32(12):2185–2190, 2013.
- ¹³M. E. Haaksma, J. M. Smit, and P. R. Tuinman. Lung ultrasound and b-lines quantification inaccuracy: "b sure to have the right solution". authors' reply. *Intensive Care Medicine*, 46(1), 2020.
- ¹⁴Y. C. Eldar, A. Ben-Tal, and A. Nemirovski. Robust mean-squared error estimation in the presence of model uncertainties. *IEEE Transactions on Signal Processing*, 53(1):168–181, 2005. doi:10.1109/TSP.2004.838933.
- ¹⁵Ningning Zhao. *Inverse problems in medical ultrasound images - applications to image deconvolution, segmentation and super-resolution*. PhD thesis, Institut National Polytechnique de Toulouse, 2016.
- ¹⁶Milica Stojadinovi, Aleksandar Filipovi, Milo Zakoek, Duan Bulatovi, and Dragan Maulovi. Lung ultrasound: Part one. *Serbian Journal of Anesthesia and Intensive Therapy*, 40(5-6):149–158, 2018.
- ¹⁷J. Ng, R. Prager, N. Kingsbury, G. Treece, and A. Gee. Modeling ultrasound imaging as a linear, shift-variant system. *IEEE Transactions on Ultrasonics, Ferroelectrics, and Frequency Control*, 53(3):549–563, 2006. doi:10.1109/TUFFC.2006.1610563.
- ¹⁸Zhao Qiang. *Medical Ultrasonic Imaging Equipment*. The Second Military Medical University Press, Shanghai, 2000.
- ¹⁹Bartosz Slak. Development, optimization and clinical evaluation of algorithms for ultrasound data analysis used in selected medical applications. <https://scholar.uwindsor.ca/etd/8339>, 2020.
- ²⁰Zhang Hua. *Clinical Analysis of Ultrasound Diagnosis of PULMONARY DISEASES*. Peking University Medical Press, Beijing, 2019.
- ²¹Ronak Raheja, Megha Brahmavar, Dhruv Joshi, and Dileep Raman. Application of lung ultrasound in critical care setting: A review. *Cureus*, 11(7), 2019.
- ²²Note1. <http://www.kangdamed.net/en/index.php/Xarioxilie/159.html>.
- ²³Note2. <http://www.kangdamed.net/en/index.php/Aplio/154.html>.
- ²⁴Note3. <https://www.sonosite.com/products>.
- ²⁵Daniel A. Lichtenstein. Blue-protocol and falls-protocol: Two applications of lung ultrasound in the critically ill. *Chest*, 2015.
- ²⁶P. H. Mayo, R. Copetti, D. Feller-Kopman, G. Mathis, and M. Zanobetti. Thoracic ultrasonography: a narrative review. *Intensive Care Medicine*, 45(6), 2019.
- ²⁷Miguel A Chavez, Navid Shams, Laura E Ellington, Neha Naithani, Robert H Gilman, Mark C Steinhoff, Mathuram Santosham, Robert E Black, Carrie Price, and Margaret and Gross. Lung ultrasound for the diagnosis of pneumonia in adults: a systematic review and meta-analysis. *Respir Res*, 15(1):50, 2014.
- ²⁸Giovanni Volpicelli, Alessandro Lamorte, and Tomás Villén. What's new in lung ultrasound during the covid-19 pandemic. *Intensive Care Medicine*, 46(4), 2020.
- ²⁹M. J. Smith, S. A. Hayward, S. M. Innes, and A. S. C. Miller. Point-of-care lung ultrasound in patients with covid-19 – a narrative review. *Anaesthesia*, 2020.
- ³⁰Niall D. Ferguson, Eddy Fan, Luigi Camporota, Massimo Antonelli, Antonio Anzueto, Richard Beale, Laurent Brochard, Roy Brower, Andrés Esteban, and Luciano and Gattinoni. The berlin

- definition of ards: an expanded rationale, justification, and supplementary material. *Intensive Care Medicine*, 38(10):1573–1582, 2012.
- ³¹Songfei Wu. Advances in the clinical application of lung ultrasonography. *Advances in Clinical Medicine*, 8(7), 2018.
- ³²Iuri Corsini, Niccolò Parri, Caterina Coviello, Valentina Leonardi, and Carlo Dani. Lung ultrasound findings in congenital diaphragmatic hernia. *Eur J Pediatr*, 2019.
- ³³Daniel A Lichtenstein. *Whole body ultrasonography in the critically ill*. Springer Science & Business Media, 2010.
- ³⁴Manifold. Ill-posed problem or inverse problem in image processing. http://blog.sina.com.cn/s/blog_6833a4df0100nne9.html, 2010.
- ³⁵A. Achim, A. Bezerianos, and P. Tsakalides. Novel bayesian multiscale method for speckle removal in medical ultrasound images. *IEEE Transactions on Medical Imaging*, 20(8):772–783, 2001. doi:10.1109/42.938245.
- ³⁶Carlos A. Duarte-Salazar, Andres E. Castro-Ospina, Miguel A. Becerra, and Edilson Delgado-Trejos. Speckle noise reduction in ultrasound images for improving the metrological evaluation of biomedical applications: An overview. *IEEE Access*, PP(99):1–1, 2020.
- ³⁷Amit Garg and Vineet Khandelwal. Segmentation based map despeckling of medical ultrasound images in shearlet domain based on normal inverse gaussian distribution. *IET Image Processing*, 14(4), 2019.
- ³⁸Hyunho Choi and Jechang Jeong. Despeckling algorithm for removing speckle noise from ultrasound images. *Symmetry*, 12(6): 1–26, 2020.
- ³⁹Yongjian Yu and S. T. Acton. Speckle reducing anisotropic diffusion. *IEEE Transactions on Image Processing*, 11(11):1260–1270, 2002. doi:10.1109/TIP.2002.804276.
- ⁴⁰Bo Chen, Yan Lv, Jinbin Zou, Wensheng Chen, and Binbin Pan. A novel speckle noise removal algorithm based on admm and energy minimization method. *Journal of Function Spaces*, 2020 (7):1–17, 2020.
- ⁴¹Stephen Boyd, Neal Parikh, and Eric Chu. *Distributed optimization and statistical learning via the alternating direction method of multipliers*. Now Publishers Inc, 2011.
- ⁴²Martino Alessandrini. Statistical methods for analysis and processing of medical ultrasound: applications to segmentation and restoration. *These de doctorat*, 2011.
- ⁴³Robinson and A. Enders. Predictive decomposition of time series with applications to seismic exploration. *Geophysics*, 32(3):418, 1967.
- ⁴⁴Ningning Zhao, Qi Wei, Adrian Basarab, Denis Kouamé, and Jean-Yves Tournet. Blind deconvolution of medical ultrasound images using a parametric model for the point spread function. In *2016 IEEE International Ultrasonics Symposium (IUS)*, pages 1–4. IEEE, 2016.
- ⁴⁵Jérôme Bolte, Shoham Sabach, and Marc Teboulle. Proximal alternating linearized minimization for nonconvex and nonsmooth problems. *Mathematical Programming*, 146(1-2):459–494, 2014.
- ⁴⁶Oleg Michailovich, Adrian Basarab, and Denis Kouame. Iterative reconstruction of medical ultrasound images using spectrally constrained phase updates. In *2019 IEEE 16th International Symposium on Biomedical Imaging (ISBI 2019)*, pages 1765–1768. IEEE, 2019.
- ⁴⁷Duong Hung Pham, Adrian Basarab, Ilyess Zemmoura, Jean Pierre Remenieras, and Denis Kouame. Joint blind deconvolution and robust principal component analysis for blood flow estimation in medical ultrasound imaging. *IEEE transactions on ultrasonics, ferroelectrics, and frequency control*, 2020.
- ⁴⁸Mohammad Talebi, Ahamd Ayatollahi, and Ali Kermani. Medical ultrasound image segmentation using genetic active contour. *Journal of Biomedical Science & Engineering*, 4(2):105–109, 2011.
- ⁴⁹Yaozhong Luo, Longzhong Liu, Qinghua Huang, and Xuelong Li. A novel segmentation approach combining region- and edge-based information for ultrasound images. *BioMed research international*, 2017.
- ⁵⁰Claudia Brusasco, Gregorio Santori, Elisa Bruzzo, Rosella Trò, Chiara Robba, Guido Tavazzi, Fabio Guarracino, Francesco Forfori, Patrizia Boccacci, and Francesco Corradi. Quantitative lung ultrasonography: a putative new algorithm for automatic detection and quantification of b-lines. *Critical Care*, 23(1):1–7, 2019.
- ⁵¹Nantheera Anantrasirichai, Wesley Hayes, Marco Allinovi, David Bull, and Alin Achim. Line detection as an inverse problem: Application to lung ultrasound imaging. *IEEE Transactions on Medical Imaging*, PP(99):1–1, 2017.
- ⁵²Oktay Karakus, Nantheera Anantrasirichai, Amazigh Aguersif, Stein Silva, Adrian Basarab, and Alin Achim. Detection of line artifacts in lung ultrasound images of covid-19 patients via nonconvex regularization. *IEEE Transactions on Ultrasonics, Ferroelectrics, and Frequency Control*, 67(11):2218–2229, Nov 2020. ISSN 1525-8955. doi:10.1109/tuffc.2020.3016092. URL <http://dx.doi.org/10.1109/TUFFC.2020.3016092>.
- ⁵³Oktay Karakus, Perla Mayo, and Alin Achim. Convergence guarantees for non-convex optimisation with cauchy-based penalties. *IEEE Transactions on Signal Processing*, 68:6159–6170, 2020.

2020. ISSN 1941-0476. doi:10.1109/tsp.2020.3032231. URL <http://dx.doi.org/10.1109/TSP.2020.3032231>.
- ⁵⁴Michael J. Bianco, Peter Gerstoft, James Traer, Emma Ozanich, Marie A. Roch, Sharon Gannot, and Charles Alban Deledalle. Machine learning in acoustics: theory and applications. *The Journal of the Acoustical Society of America*, 146(5):3590–3628, 2019.
- ⁵⁵Massimo Mischi, Muyinatu A. Lediju Bell, Ruud J. G. Van Sloun, and Yonina C. Eldar. Deep learning in medical ultrasound—from image formation to image analysis. *IEEE Transactions on Ultrasonics Ferroelectrics and Frequency Control*, 67(12):2477–2480, 2020.
- ⁵⁶Jong Chul Ye and Yo Seob Han. Deep convolutional framelets: A general deep learning for inverse problems. *SIAM Journal on Imaging Sciences*, 11(2), 2017.
- ⁵⁷Harshit Gupta. From classical to unsupervised-deep-learning methods for solving inverse problems in imaging. *PhD Dissertation*, page 195, 2020. doi:10.5075/epfl-thesis-7360. URL <http://infoscience.epfl.ch/record/280353>.
- ⁵⁸Shengfeng Liu, Yi Wang, Xin Yang, Shawn Li, Tianfu Wang, Baiying Lei, Dong Ni, and Li Liu. Deep learning in medical ultrasound analysis: A review. *Engineering*, 5:261–275, 03 2019. doi:10.1016/j.eng.2018.11.020.
- ⁵⁹Muhammad Razzak, Saeeda Naz, and Ahmad Zaib. Deep learning for medical image processing: Overview, challenges and future. *Classification in BioApps*, pages 323–350, 2018.
- ⁶⁰Alice Lucas, Michael Iliadis, Rafael Molina, and Aggelos K. Katsaggelos. Using deep neural networks for inverse problems in imaging: Beyond analytical methods. *IEEE Signal Processing Magazine*, 35(1):20–36, 2018.
- ⁶¹Kyong Hwan Jin, Michael T. Mccann, Emmanuel Froustey, and Michael Unser. Deep convolutional neural network for inverse problems in imaging. *IEEE Transactions on Image Processing*, PP(99):4509–4522, 2016.
- ⁶²Olaf Ronneberger, Philipp Fischer, and Thomas Brox. U-net: Convolutional networks for biomedical image segmentation. In *International Conference on Medical image computing and computer-assisted intervention*, pages 234–241. Springer, 2015.
- ⁶³J. H. Rick Chang, Chun Liang Li, Barnabas Poczos, B. V. K. Vijaya Kumar, and Aswin C Sankaranarayanan. One network to solve them all — solving linear inverse problems using deep projection models. In *Proceedings of the IEEE International Conference on Computer Vision*, pages 5888–5897, 2017.
- ⁶⁴Jonathan I. Tamir, Stella X. Yu, and Michael Lustig. Unsupervised deep basis pursuit: Learning inverse problems without ground-truth data, 2020.
- ⁶⁵Dmitry Ulyanov, Andrea Vedaldi, and Victor Lempitsky. Deep image prior. In *Proceedings of the IEEE conference on computer vision and pattern recognition*, pages 9446–9454, 2018.
- ⁶⁶He Sun and Katherine L. Bouman. Deep probabilistic imaging: Uncertainty quantification and multi-modal solution characterization for computational imaging, 2020.
- ⁶⁷Rushil Anirudh, Jayaraman J. Thiagarajan, B. Kailkhura, and T. Bremer. An unsupervised approach to solving inverse problems using generative adversarial networks. *ArXiv*, abs/1805.07281, 2018.
- ⁶⁸Razvan V Marinescu, Daniel Moyer, and Polina Golland. Bayesian image reconstruction using deep generative models, 2021.
- ⁶⁹R. J. G. van Sloun, R. Cohen, and Y. C. Eldar. Deep learning in ultrasound imaging. *Proceedings of the IEEE*, 108(1):11–29, 2020. doi:10.1109/JPROC.2019.2932116.
- ⁷⁰Sanketh Vedula, Ortal Senouf, Alex M. Bronstein, Oleg V. Michailovich, and Michael Zibulevsky. Towards ct-quality ultrasound imaging using deep learning, 2017.
- ⁷¹Danlei Feng, Weichen Wu, Hongfeng Li, and Quanzheng Li. *Speckle Noise Removal in Ultrasound Images Using a Deep Convolutional Neural Network and a Specially Designed Loss Function*, pages 85–92. Springer Nature Switzerland AG, Switzerland, 01 2020. ISBN 978-3-030-37968-1. doi:10.1007/978-3-030-37969-8_11.
- ⁷²Hongliang Li, Tal Mezheritsky, Liset Vazquez Romaguera, and Samuel Kadoury. 3d b-mode ultrasound speckle reduction using deep learning for 3d registration applications. *arXiv preprint arXiv:2008.01147*, 2020.
- ⁷³Dimitris Perdios, Adrien Besson, Marcel Arditi, and Jean-Philippe Thiran. A deep learning approach to ultrasound image recovery. In *2017 IEEE International Ultrasonics Symposium (IUS)*, pages 1–4. Ieee, 2017.
- ⁷⁴Yeo Hun Yoon and Jong Chul Ye. Deep learning for accelerated ultrasound imaging. In *2018 IEEE International Conference on Acoustics, Speech and Signal Processing (ICASSP)*, pages 6673–6676. IEEE, 2018.
- ⁷⁵Vibhakar Shrimali Fiete, R. S. Anand, Vinod Kumar Senior Member, and IEEE. Current trends in segmentation of medical ultrasound b-mode images: A review. *Iete Technical Review*, 26(1):8–17, 2009.
- ⁷⁶Tao Lei, Risheng Wang, Yong Wan, Xiaogang Du, and Asoke K. Nandi. Medical image segmentation using deep learning: A survey. *arXiv preprint arXiv:2009.13120*, 2020.

- ⁷⁷Hao Dong, Guang Yang, Fangde Liu, Yuanhan Mo, and Yike Guo. Automatic brain tumor detection and segmentation using u-net based fully convolutional networks. In María Valdés Hernández and Víctor González-Castro, editors, *Medical Image Understanding and Analysis*, pages 506–517, Cham, 2017. Springer International Publishing. ISBN 978-3-319-60964-5.
- ⁷⁸Dwarikanath Mahapatra, Behzad Bozorgtabar, Jean-Philippe Thiran, and Mauricio Reyes. Efficient active learning for image classification and segmentation using a sample selection and conditional generative adversarial network. In *International Conference on Medical Image Computing and Computer-Assisted Intervention*, pages 580–588. Springer, 2018.
- ⁷⁹Pierre-Henri Conze, Sylvain Brochard, Valérie Burdin, Frances T Sheehan, and Christelle Pons. Healthy versus pathological learning transferability in shoulder muscle mri segmentation using deep convolutional encoder-decoders. *Computerized Medical Imaging and Graphics*, 83:101733, 2020.
- ⁸⁰Cheng Chen, Qi Dou, Hao Chen, Jing Qin, and Pheng-Ann Heng. Synergistic image and feature adaptation: Towards cross-modality domain adaptation for medical image segmentation. In *Proceedings of the AAAI Conference on Artificial Intelligence*, volume 33, pages 865–872, 2019.
- ⁸¹Guotai Wang, Maria A Zuluaga, Wenqi Li, Rosalind Pratt, Premal A Patel, Michael Aertsen, Tom Doel, Anna L David, Jan Deprest, Sébastien Ourselin, et al. Deepigeos: a deep interactive geodesic framework for medical image segmentation. *IEEE transactions on pattern analysis and machine intelligence*, 41(7): 1559–1572, 2018.
- ⁸²Guotai Wang, Wenqi Li, Maria A Zuluaga, Rosalind Pratt, Premal A Patel, Michael Aertsen, Tom Doel, Anna L David, Jan Deprest, Sébastien Ourselin, et al. Interactive medical image segmentation using deep learning with image-specific fine tuning. *IEEE transactions on medical imaging*, 37(7):1562–1573, 2018.
- ⁸³Christian Rupprecht, Iro Laina, Nassir Navab, Gregory D. Hager, and Federico Tombari. Guide me: Interacting with deep networks, 2018.
- ⁸⁴Junyu Chen and E. Frey. Medical image segmentation via unsupervised convolutional neural network. *arXiv: Computer Vision and Pattern Recognition*, 2020.
- ⁸⁵Ziyang Wang, Zhang Zhengdong, Zheng Jianqing, Huang Baoru, Voiculescu Irina, and Yang GuangZhong. Deep learning in medical ultrasound image segmentation: a review. *arXiv preprint arXiv:2002.07703*, 2020.
- ⁸⁶Conor McDermott, Maciej Łacki, Ben Sainsbury, Jessica Henry, Mihail Filippov, and Carlos Rossa. Sonographic diagnosis of covid-19: A review of image processing for lung ultrasound. *Frontiers in Big Data*, 4:2, 2021. ISSN 2624-909X. doi: 10.3389/fdata.2021.612561. URL <https://www.frontiersin.org/article/10.3389/fdata.2021.612561>.
- ⁸⁷Sourabh Kulhare, Xinliang Zheng, Courosh Mehanian, Cynthia Gregory, Meihua Zhu, Kenton Gregory, Hua Xie, James McAndrew Jones, and Benjamin Wilson. Ultrasound-based detection of lung abnormalities using single shot detection convolutional neural networks. In *Simulation, Image Processing, and Ultrasound Systems for Assisted Diagnosis and Navigation*, pages 65–73. Springer, 2018.
- ⁸⁸Ruud Jg Van Sloun and Libertario Demi. Localizing b-lines in lung ultrasonography by weakly supervised deep learning, in-vivo results. *IEEE Journal of Biomedical and Health Informatics*, PP (99), 2019.
- ⁸⁹Xianglong Wang, Joseph S. Burzynski, James Hamilton, Panduranga S. Rao, William F. Weitzel, and Joseph L. Bull. Quantifying lung ultrasound comets with a convolutional neural network: Initial clinical results. *Computers in Biology and Medicine*, 2019.
- ⁹⁰Aitor Almeida, Aritz Bilbao, Lisa Ruby, Marga B Rominger, Diego López-De-Ipiña, Jeremy Dahl, Ahmed ElKaffas, and Sergio J Sanabria. Lung ultrasound for point-of-care covid-19 pneumonia stratification: computer-aided diagnostics in a smartphone. first experiences classifying semiology from public datasets. In *2020 IEEE International Ultrasonics Symposium (IUS)*, pages 1–4. IEEE, 2020.
- ⁹¹Jannis Born, Gabriel Brändle, Manuel Cossio, Marion Disdier, Julie Goulet, Jérémie Roulin, and Nina Wiedemann. Pocusnet: Automatic detection of covid-19 from a new lung ultrasound imaging dataset (pocus), 2020.
- ⁹²Subhankar Roy, Willi Menapace, Sebastiaan Oei, Ben Luijten, and Libertario Demi. Deep learning for classification and localization of covid-19 markers in point-of-care lung ultrasound. *IEEE Transactions on Medical Imaging*, PP(99), 2020.
- ⁹³Note4. <https://iclus-web.bluetensor.ai>.
- ⁹⁴Max Jaderberg, Karen Simonyan, Andrew Zisserman, and Koray Kavukcuoglu. Spatial transformer networks, 2016.
- ⁹⁵C. Baloesu, G. Toporek, S. Kim, K. McNamara, R. Liu, M. M. Shaw, R. L. McNamara, B. I. Raju, and C. L. Moore. Automated lung ultrasound b-line assessment using a deep learning algorithm. *IEEE Transactions on Ultrasonics, Ferroelectrics, and Frequency Control*, 67(11):2312–2320, 2020. doi:

10.1109/TUFFC.2020.3002249.

⁹⁶Senthil Kumar Veeramani and Ezhilarasi Muthusamy. Detection of abnormalities in ultrasound lung image using multi-level rvm classification. *The Journal of Maternal-Fetal & Neonatal Medicine*, 2015.

⁹⁷Michael. J. Horry, Subrata Chakraborty, Manoranjan Paul, Anwaar Ulhaq, and Nagesh Shukla. Covid-19 detection through transfer learning using multimodal imaging data. *IEEE Access*, PP(99):1–1, 2020.